

<https://doi.org/10.1038/s41612-025-01253-z>

On the Atlantic extratropical-tropical teleconnection in response to external freshwater forcing

Check for updates

Rajat Joshi¹ ✉ & Rong Zhang^{1,2} ✉

We investigate key mechanisms driving the Atlantic extratropical-tropical teleconnection and associated Atlantic Intertropical Convergence Zone (ITCZ) shift in boreal summer under a strong external freshwater forcing using a coupled climate model. Our analysis reveals that the wind-evaporation-sea surface temperature (SST) feedback is not the primary mechanism. Instead, the southward advection of the upper extratropical North Atlantic signal by the North Atlantic subtropical gyre along a horseshoe pathway is a key mechanism for forming the horseshoe pattern of cold SST anomalies. Additionally, the weakening of the Atlantic Meridional Overturning Circulation changes the upper tropical North Atlantic western boundary current. This change is amplified by enhanced surface wind stress curl over the tropical North Atlantic, contributing to warmer tropical Atlantic subsurface thermocline temperature and SST in the tropical South Atlantic. The dipole Atlantic SST anomalies lead to the trade wind response and associated southward ITCZ shift over the tropical Atlantic.

The Atlantic Meridional Overturning Circulation (AMOC) plays an important role in the global climate system^{1–3}. Due to limited observations, climate models are often used to study the teleconnection associated with the AMOC weakening induced by external freshwater forcing applied over northern high latitudes. Many modeling studies suggest that external freshwater forcing weakens the AMOC, leading to a significant cooling (warming) in the sea surface temperature (SST) in the North (South) Atlantic and a southward shift of the Atlantic Intertropical Convergence Zone (ITCZ) during boreal summer^{4–6}. The surface cooling spreads equatorward from the extratropical North Atlantic, forming a distinctive horseshoe pattern in the North Atlantic SST anomalies^{5,6}. The horseshoe pattern in the North Atlantic SST anomalies is evident not only in climate model simulations, but also in observed SST anomalies associated with Atlantic Multidecadal Variability (AMV^{3,7}), where SST anomalies propagate from the extratropical North Atlantic into the tropical North Atlantic along a horseshoe pathway⁷ and induce the Atlantic ITCZ shift and Sahel rainfall response during boreal summer^{8,9}.

The subpolar North Atlantic has been identified as a crucial source region for predicting the southward shift of the Atlantic ITCZ through the Atlantic extratropical-tropical teleconnection¹⁰. Despite its importance, the mechanisms of the Atlantic extratropical-tropical teleconnection and how the extratropical North Atlantic changes affect boreal summer Atlantic ITCZ shift remain poorly understood. Additionally, the AMOC/AMV-

related tropical Atlantic SST signal and associated boreal summer Atlantic ITCZ shift/Sahel rainfall response are often underestimated in climate models^{5,11–13}. The energy budget framework, which involves a compensation between cross-equatorial northward ocean and atmosphere heat transport, is often used in previous studies to explain the extratropical-tropical teleconnection and associated ITCZ shift^{5,14–16}. However, the zonally integrated energy budget framework does not account for the formation of the zonally asymmetric North Atlantic SST horseshoe pattern with relatively stronger response propagating through the eastern boundary of the North Atlantic subtropical gyre, a key feature of the Atlantic extratropical-tropical teleconnection.

Previous studies often attribute the equatorward propagation of cold extratropical SST anomalies to the positive Wind-Evaporation-SST (WES) feedback^{17,18}. However, these findings are often based on modeling results from atmospheric general circulation models (AGCMs) coupled to slab ocean models without ocean dynamics. Meanwhile, studies based on models with ocean dynamics suggest that the reduced dense water formation at northern high latitudes in response to external freshwater forcing induces equatorward propagation of coastal Kelvin waves along the North Atlantic western boundary, continued eastward propagation along the equator as Kelvin waves, and partially westward propagation as Rossby waves in the tropical Atlantic, which are indicated partly by the thermocline deepening and warm thermocline temperature anomalies along these

¹Program in Atmospheric and Oceanic Sciences, Princeton University, Princeton, NJ, USA. ²NOAA/OAR/GFDL, Princeton, NJ, USA.

✉ e-mail: rajatjoshi@princeton.edu; rong.zhang@noaa.gov

propagation pathways^{19,20}. When the AMOC weakening is strong enough, the zonally integrated meridional overturning streamfunction across the upper tropical North Atlantic is dominated by the wind-driven northern subtropical cell (NSTC)²¹. Hence the equatorward subsurface return flow of the NSTC becomes visible, which has been proposed to accelerate the tropical Atlantic subsurface warming/South Atlantic surface warming and reduced monsoon rainfall over West Africa during boreal summer²¹. It remains unclear if there is any coupled positive feedback between responses in ocean and atmosphere circulation over the tropical Atlantic. A better understanding of the mechanisms that drive the Atlantic extratropical-tropical teleconnection is crucial for accurately predicting the associated tropical atmospheric response with profound socioeconomic implications.

Here using a fully coupled climate model^{22,23}, we conduct an idealized water hosing ensemble with 0.6 Sv of external freshwater forcing applied over the southern Nordic Seas for 80 years (see “Methods” section) to investigate mechanisms of the Atlantic extratropical-tropical teleconnection under strong external freshwater forcing. Our analysis is focused on boreal summer, during which the southward Atlantic ITCZ shift is most pronounced. The identified mechanisms will help explain why many climate models underestimate the AMOC-related tropical Atlantic SST anomalies and associated boreal summer Atlantic ITCZ shift.

Results

Anomalies in the annual mean AMOC and global heat transport

In the water hosing ensemble, the maximum annual mean AMOC strength at 26.5°N declines rapidly within the first 40 years, from ~16 Sv in the control ensemble to ~3 Sv (Fig. 1a). After this rapid initial decline, the weakened AMOC stabilizes and reaches a quasi-equilibrium state over the last 40 years (Fig. 1a). Associated with the weakened AMOC in this quasi-equilibrium state is a reduction in the annual mean northward global ocean heat transport, which decreases by ~0.4 PW (Fig. 1b). This decrease in the annual mean cross-equatorial northward global ocean heat transport is overcompensated by an increase in the annual mean cross-equatorial northward global atmosphere heat transport of ~0.5 PW (Fig. 1b), similar to that found in previous water hosing experiments⁵. The enhanced annual mean cross-equatorial northward global atmosphere heat transport is associated with a strong anomalous clockwise annual mean Hadley cell (Fig. 1c, d), extending from ~20°S to ~20°N, consistent with previous findings⁵. As shown in the previous study⁵, the above global zonally integrated energy budget framework is consistent with the anomalous clockwise annual mean Hadley cell response and associated annual mean southward ITCZ shift. While the global zonally integrated Hadley circulation exhibits an anomalous clockwise circulation of a similar strength in both boreal summer and winter, the vertical motion response over the Atlantic basin is

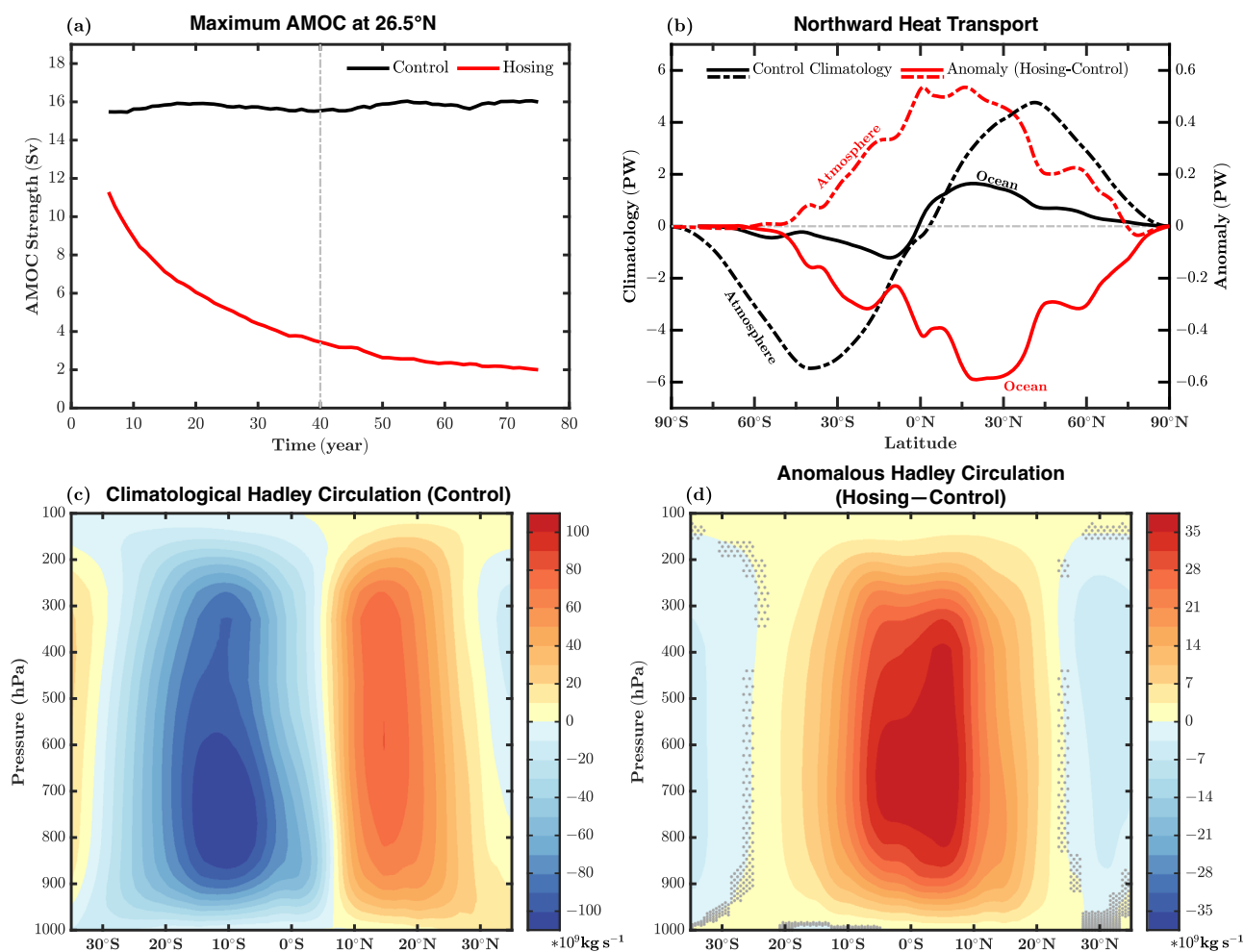


Fig. 1 | The maximum AMOC strength, climatological mean global northward ocean/atmosphere heat transport and Hadley cell along with the long-term mean anomalies. a Time series of the annual mean maximum AMOC streamfunction at 26.5°N for the control (black) and hosing (red) ensembles, derived from the 11-year running mean of the ensemble mean. **b** The climatology (black) and anomaly (hosing minus control in red) of the annual mean global northward ocean (solid lines) and atmosphere (dashed lines) heat transport (PW), averaged over the last 40

years of all ensembles. **c** Climatology of annual mean Hadley cell (zonally integrated atmosphere streamfunction; 10^9 kg s^{-1}) for the control ensemble (averaged over the last 40 years). **d** Anomalous annual mean Hadley cell, where the anomaly is the ensemble mean difference between the hosing and the control ensembles averaged over the last 40 years. The stippling in **(d)** (gray color) indicates the regions where the Hadley cell anomaly is not significant at the 5% level.

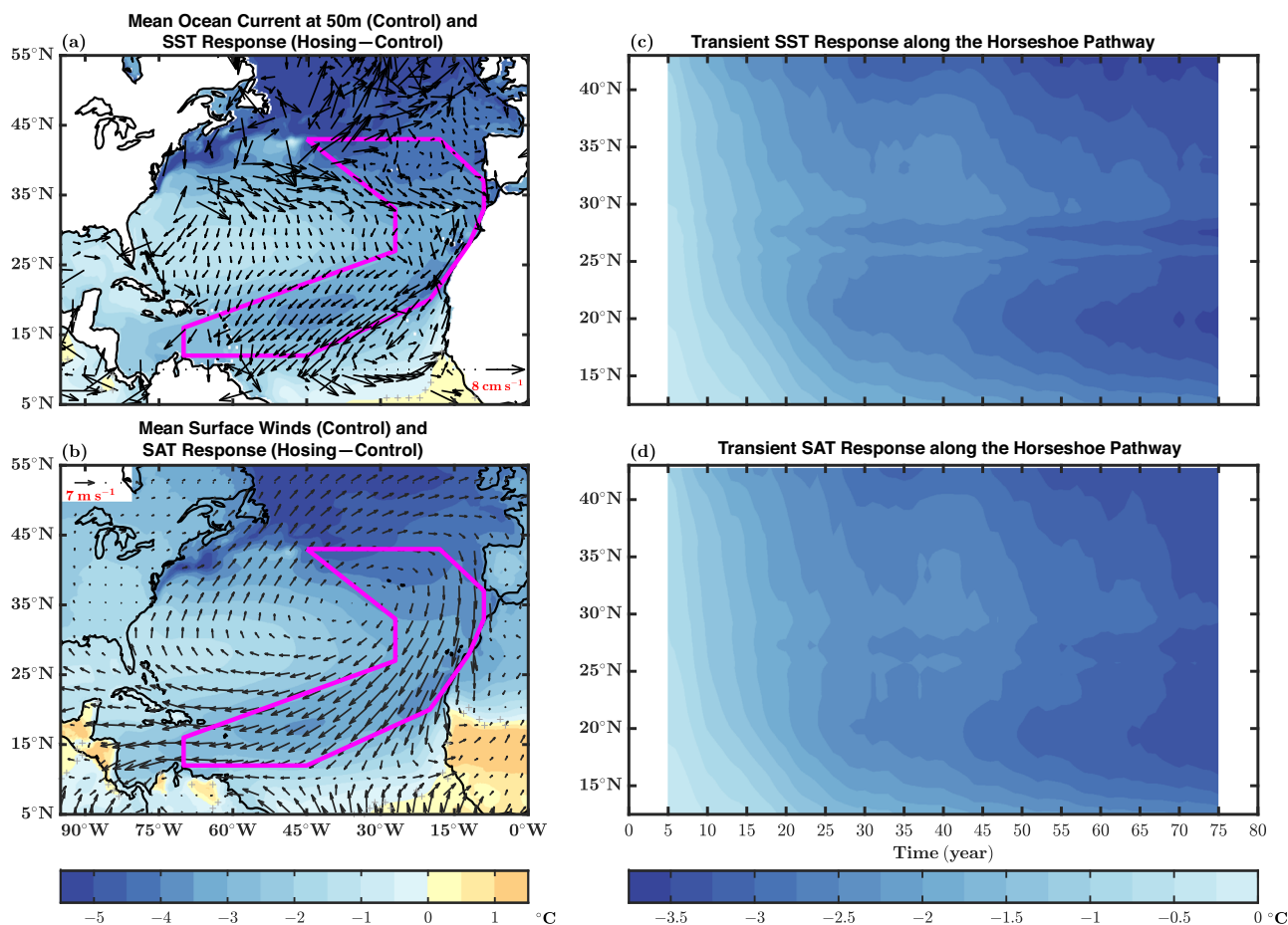


Fig. 2 | Boreal summer climatological mean circulation for the control ensemble and SST/SAT response for the hosing ensemble. a Climatological mean ocean current (vector) at 50 m overlapped with long-term mean SST response (shading). Vectors larger than 8 cm s^{-1} in magnitude are not shown. **b** Climatological mean 10-m winds (vector) overlapped with long-term mean surface air temperature (SAT) response (shading). The climatological mean ocean and atmospheric circulation are calculated from the control ensemble averaged over boreal summer (June through

September; JJAS) of the last 40 years. The response in (a, b) is the ensemble mean differences between the hosing and the control ensembles, averaged over boreal summer of the last 40 years. Gray stippling in (a, b) indicates regions where the SST/SAT response is not statistically significant at the 5% level. **c, d** 11-year running mean of transient SST and SAT response along the horseshoe pathway (averaged within the magenta box). The transient response in (c, d) is the ensemble mean difference between the hosing and the control ensembles, averaged over boreal summer.

weaker in boreal winter than in boreal summer (Supplementary Fig. 1), consistent with a weaker Atlantic ITCZ shift in boreal winter than in boreal summer that is not reflected in the global integrated Hadley circulation anomaly. The subsidence response over the Atlantic basin is largely confined to the deep tropics, with weaker subsidence response over the subtropics, especially during boreal winter (Supplementary Fig. 1c, d).

While the zonally integrated energy budget framework provides a context for interpreting the quasi-equilibrium energy balance under the AMOC weakening, it does not explain the key mechanisms/processes for the transient evolution of the zonally asymmetric North Atlantic SST horseshoe pattern with relatively stronger response propagating through the eastern boundary of the North Atlantic subtropical gyre, a key feature of the Atlantic extratropical-tropical teleconnection.

The boreal summer cold SST/SAT anomalies over the North Atlantic along the horseshoe pathway

In the water hosing ensemble characterized by a weakened AMOC compared to the control ensemble, a distinct quasi-equilibrium horseshoe pattern of boreal summer cold SST anomalies is established in the North Atlantic (Fig. 2a). The cold SST anomalies are stronger in the extratropical North Atlantic (Fig. 2a), primarily due to reduced northward Atlantic Ocean heat transport (Supplementary Fig. 2) associated with the weakening of the North Atlantic Current (Supplementary Fig. 3) in response to the AMOC weakening under external freshwater forcing, as found in previous

studies^{5,24–27}. To balance the reduction in the Atlantic Ocean heat transport convergence over the extratropical North Atlantic, the net downward surface heat flux (F_{SFC}) over most regions of the extratropical North Atlantic consistently exhibits positive anomalies (i.e., less surface air–sea heat flux released into the atmosphere and more air–sea heat flux entering into the ocean, Fig. 3b). Hence the F_{SFC} response provides negative feedback (i.e., damping effect) to the cold extratropical North Atlantic SST anomalies and drives the cold surface air temperature (SAT) anomalies over the extratropical North Atlantic (Fig. 2b).

The cold extratropical North Atlantic SST anomalies first appear in the extratropical North Atlantic and gradually propagate equatorward (Fig. 2c), forming the characteristic zonally asymmetric North Atlantic SST horseshoe pattern with relatively stronger response propagating through the eastern boundary of the North Atlantic subtropical gyre (Fig. 2a). The cold SAT anomalies over the North Atlantic exhibit a similar zonally asymmetric horseshoe pattern (Fig. 2b), indicating a potential coupled ocean-atmosphere interaction between these cold SST and SAT anomalies. However, the mechanisms behind the formation of the boreal summer zonally asymmetric North Atlantic SST/SAT horseshoe pattern remain poorly understood. To investigate these processes, we focus on the region from the extratropical North Atlantic to the tropical North Atlantic along the “horseshoe pathway” (magenta box in Fig. 2a, b).

During the first decade (years 1–10), there is a weak equatorward spread of the extratropical cooling (Fig. 4a). The net downward surface heat

Boreal Summer Long-term Mean Response (Hosing—Control)

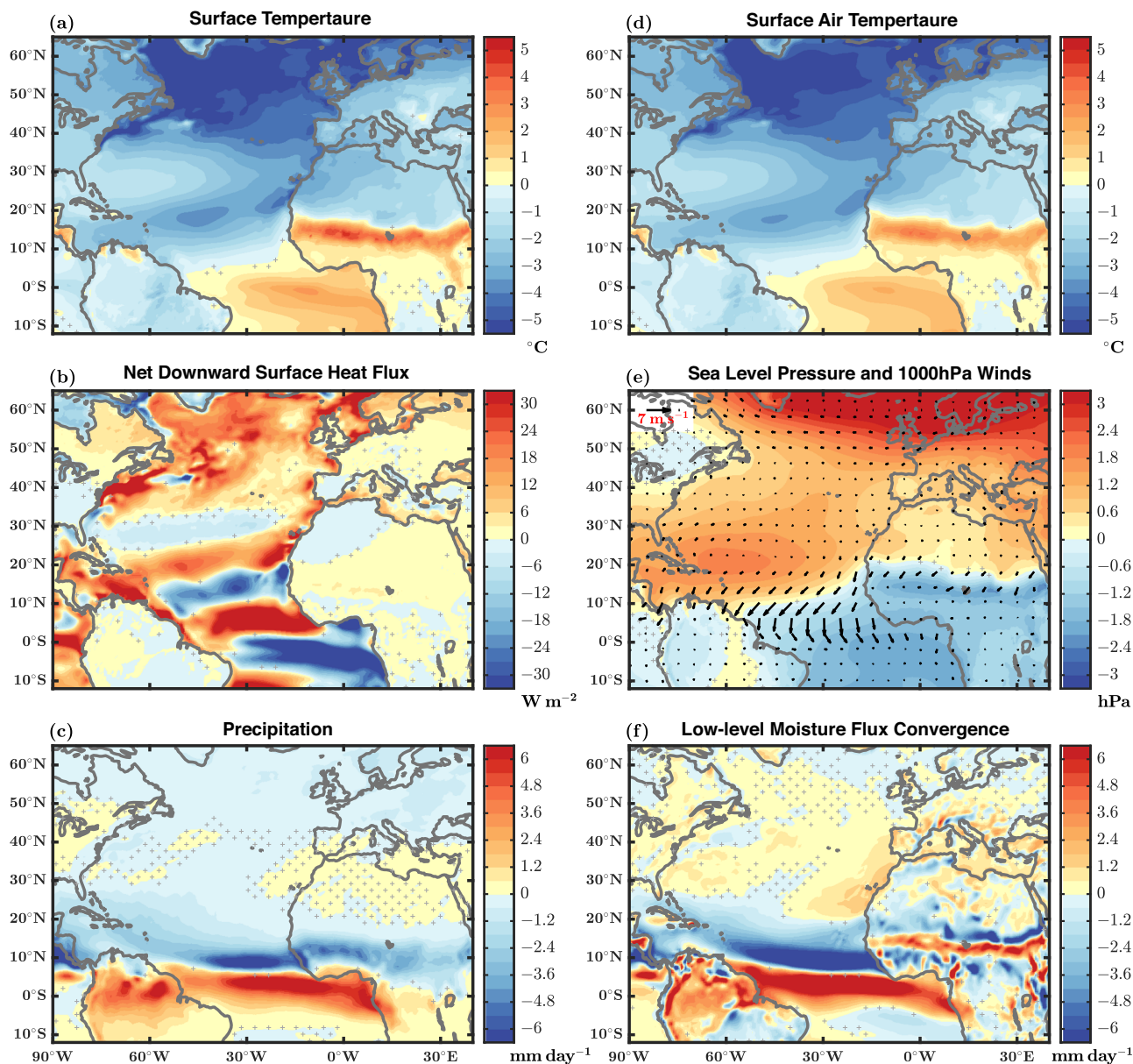


Fig. 3 | Long-term mean boreal summer response. The response is the ensemble mean difference between the hosing and the control ensembles averaged over boreal summer (JJAS) of the last 40 years. **a–c** Response in surface temperature, net downward surface heat flux, and precipitation. **d–f** Response in surface air

temperature, sea level pressure (shading), 1000 hPa winds (vector), and low-level moisture flux convergence (See “Methods”). Gray stippling indicates regions where the response shown in shading is not statistically significant at the 5% level.

flux (F_{SFC}) response along the horseshoe pathway during this period is negative (extracting more heat from the ocean) south of 30°N (Fig. 4e), suggesting a role of atmospheric cooling in the initial weak equatorward spread of the extratropical SST anomalies, particularly south of 30°N. This early-stage equatorward spread of the weak extratropical signal is likely affected by the fast advection/spread of the cold extratropical surface air temperature (SAT) anomalies equatorward (Fig. 2d) by the climatological mean atmospheric subtropical anticyclone (Fig. 2b), which contributes to the SST anomalies through air–sea heat flux exchange. Meanwhile, changes in the surface wind along the subtropical horseshoe pathway is very small (Fig. 4a).

The temporal evolution of the SST response along the horseshoe pathway gradually reveals a noticeable delay in the equatorward propagation of cold extratropical North Atlantic SST anomalies (Fig. 2c), suggesting

the involvement of slow oceanic processes, in contrast to fast (almost in phase) atmospheric processes. From the second decade onward (i.e., years 11–20 and onwards), the equatorward spread of the cold extratropical SST anomalies along the horseshoe pathway becomes more pronounced (Fig. 4b–d). Concurrently, the F_{SFC} anomalies along the eastern side of the horseshoe pathway switch sign and become consistently positive (i.e., more heat flux entering into the ocean, Fig. 4f–h). Hence, from the second decade onward, the F_{SFC} response provides negative feedback (i.e., damping effect) to the cold SST anomalies and contributes to the cold SAT anomalies along the eastern side of the horseshoe pathway, suggesting a dominant role of the slow oceanic processes in shaping the SST/SAT anomalies along the eastern side of the horseshoe pattern (Fig. 4b–d). The climatological mean boreal summer upper ocean horizontal circulation in the subtropical North Atlantic is characterized by an anticyclonic gyre (i.e., the North Atlantic

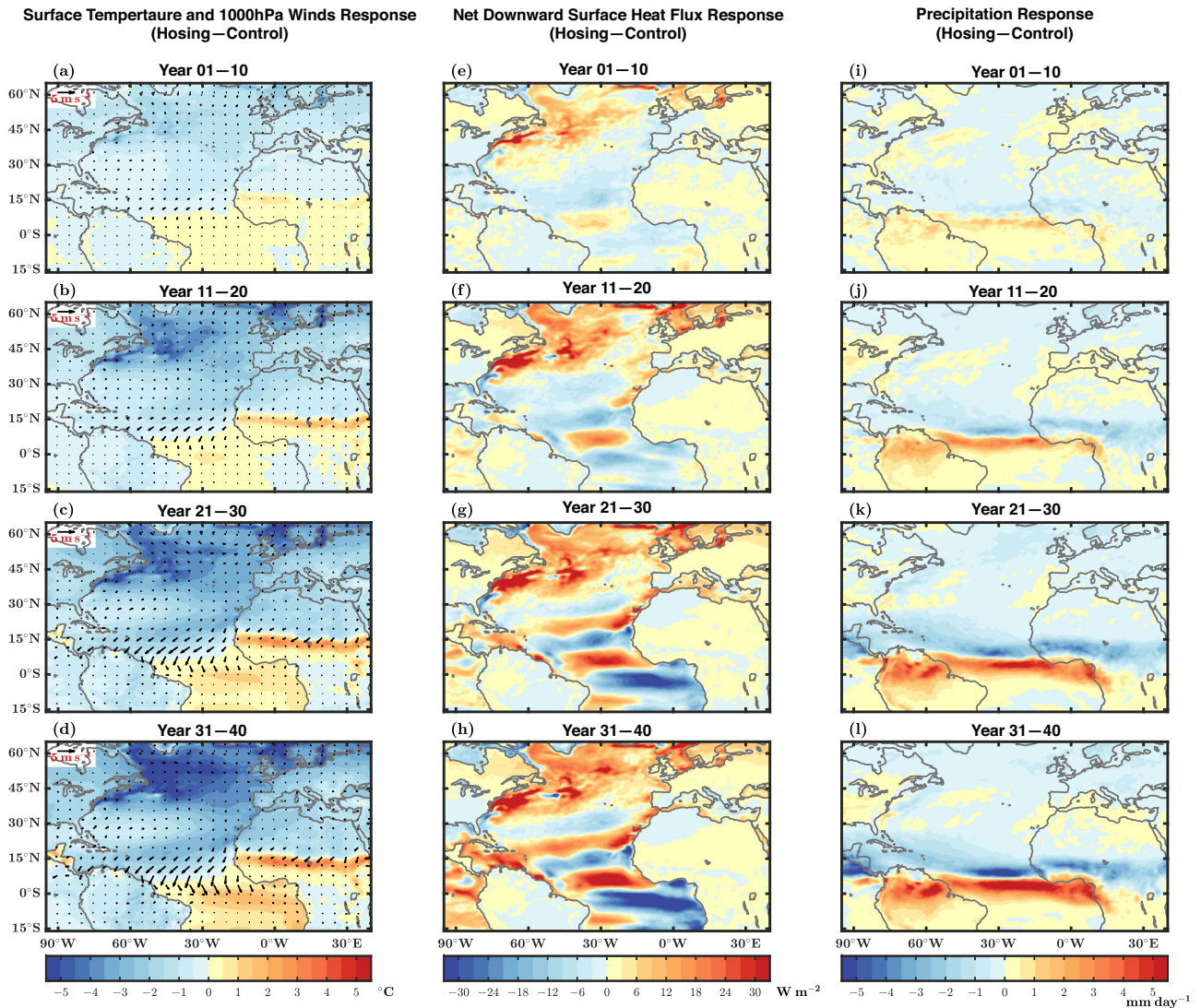


Fig. 4 | Transient boreal summer response in surface temperature/winds/net downward heat flux and precipitation. The response is the ensemble mean difference between the hosing and the control ensembles, averaged over boreal summer

(JJAS) of years 01–10, 11–20, 21–30, and 31–40. **a–d** Surface temperature response (shading) overlapped with near-surface winds response (vector). **e–h** Net downward surface heat flux response. **i–l** Precipitation response.

subtropical gyre; Fig. 2a), and its eastern branch aligns well with the horseshoe pathway for the equatorward spread of the extratropical surface cooling (Fig. 2a). This suggests that the equatorward advection of the cold extratropical SST anomalies by the eastern branch of the climatological mean North Atlantic subtropical gyre is potentially important for the formation of the North Atlantic SST horseshoe pattern.

The temporal evolution of negative sea surface salinity (SSS) anomalies along the horseshoe pathway further supports the importance of the slow oceanic advection in transmitting the extratropical North Atlantic signal toward the tropics in the water hosing ensemble (Fig. 5a–d). The negative SSS anomalies, initially concentrated in the extratropical North Atlantic (primarily due to the advection of externally forced freshwater anomalies by the western boundary current in the subpolar North Atlantic and the mixing of these freshwater anomalies into the interior ocean), do not show a clear equatorward propagation along the horseshoe pathway during the first decade (Fig. 5a). They exhibit an equatorward propagation along the northeastern branch of the North Atlantic subtropical gyre (i.e., the northern branch of the horseshoe pathway) by the second decade (Fig. 5b). As the negative extratropical SSS anomalies become stronger by the third and fourth decades, pronounced negative SSS anomalies also appear along the southeastern branch of the North Atlantic subtropical gyre (i.e., the southern branch of the horseshoe pathway), forming a horseshoe pattern

(Fig. 5c, d). This transient response reveals a key role of the eastern branch of the climatological mean North Atlantic subtropical gyre in advecting the extratropical oceanic signal towards the tropics and ultimately shaping the North Atlantic horseshoe pattern in both SST and SSS anomalies (Fig. 3a, Supplementary Fig. 4a). The boreal summer mixed layer depth along the horseshoe pathway is slightly reduced (by the order of ~5–7 m) due to the negative SSS anomalies, which would provide some negative feedback to the SST cooling along the horseshoe pathway.

In the water hosing ensemble, there is a similar advection of negative extratropical upper ocean temperature/salinity anomalies by the eastern branch of the climatological mean North Atlantic subtropical gyre along the horseshoe pathway (Supplementary Fig. 5a–h). These negative temperature and salinity anomalies have a compensating effect on density anomalies, and the negative upper ocean density anomalies along the horseshoe pathway are dominated by the pronounced negative upper ocean salinity anomalies (Supplementary Fig. 5i–l). Consistently, there are growing positive anomalies of the sea surface height (SSH) above the geoid along the horseshoe pathway (Fig. 5e–h), which strengthens the eastern branch of the upper North Atlantic subtropical gyre (where the gradient of positive anomalies of the SSH above geoid is largest). Hence, the southwestward upper ocean current along the southern horseshoe pathway becomes strengthened (Supplementary Fig. 4b), which corresponds to an enhanced

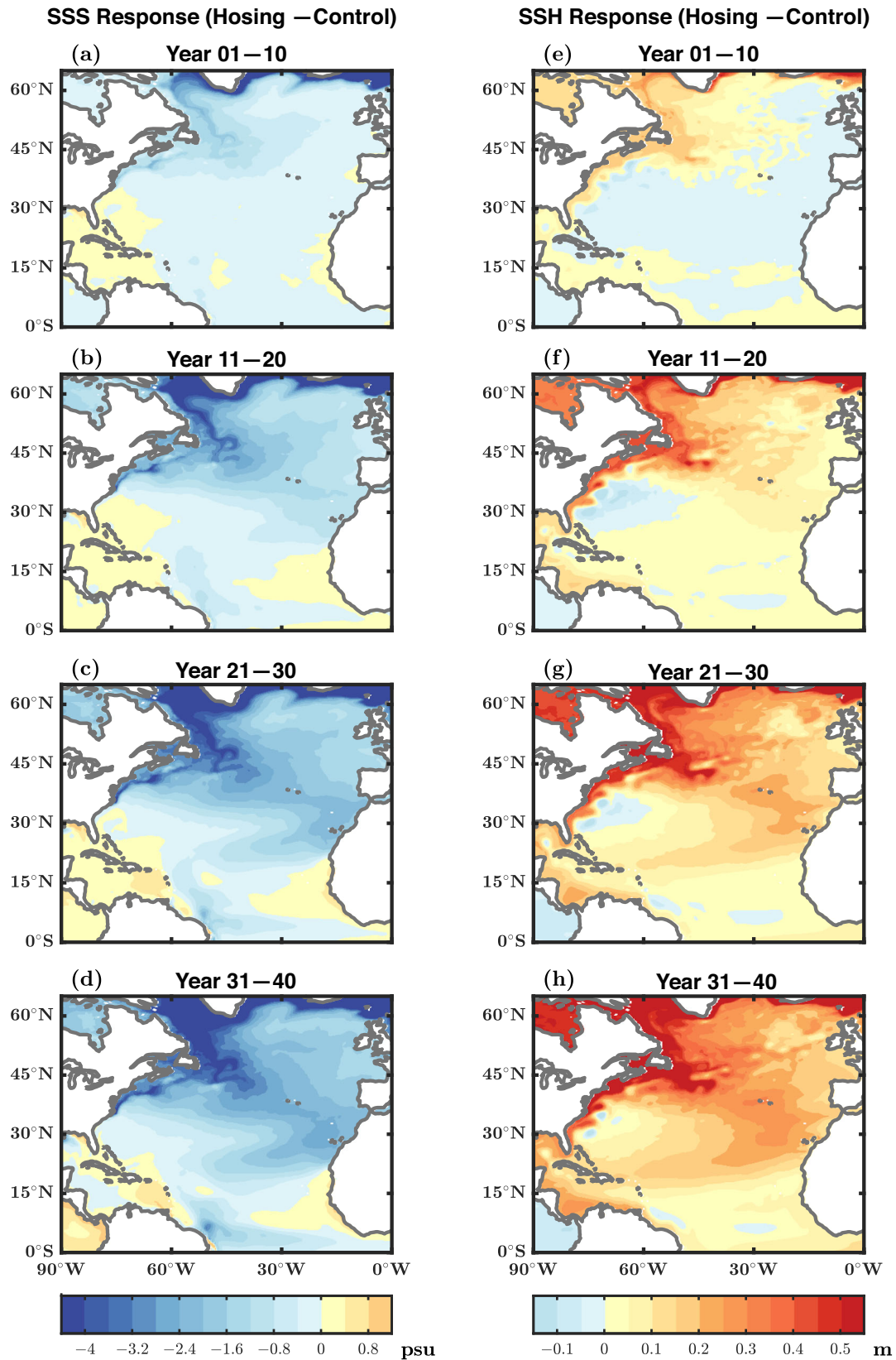


Fig. 5 | Transient boreal summer response in SSS and SSH. The response is derived in the same way as in Fig. 4. **a–d** Sea surface salinity (SSS) response. **e–h** Sea surface height (SSH) response above the geoid.

divergence of the vertically integrated upper ocean horizontal velocity along the eastern boundary and thus enhanced eastern boundary upwelling (Supplementary Fig. 6). The enhanced eastern boundary upwelling leads to enhanced upper ocean cooling near the eastern boundary (Supplementary Fig. 5a–d), which is advected southwestward along the southern horseshoe pathway by the mean and strengthened southwestward ocean currents, contributing to the enhanced ocean heat transport divergence and amplified cold upper-ocean temperature anomalies over the southern horseshoe pathway (Supplementary Figs. 4c, 5a–d). The enhanced ocean heat transport divergence is evident/reflected by the enhanced F_{SFC} that is in balance with it over the southern horseshoe pathway (Fig. 3b). The enhanced eastern branch of the upper North Atlantic subtropical gyre (Supplementary Fig. 4b) also advects the cold extratropical SST anomalies along the horseshoe pathway from the northeastern boundary of the North Atlantic subtropical gyre, in addition to the advection by the mean upper North Atlantic subtropical gyre.

An earlier study suggests that the F_{SFC} response to changes in the AMOC can vary significantly with the season and the response during boreal summer could be due to the accumulated F_{SFC} anomalies during boreal winter²⁸. Our experiments do not show such seasonal reversal in the net downward surface heat flux anomalies along the North Atlantic horseshoe pathway (Supplementary Fig. 7a, b). During both boreal summer and winter, the F_{SFC} response along the horseshoe pathway provides negative feedback (i.e., damping effect) to the SST anomalies (Supplementary Fig. 7a, b). Although boreal winter tropical Atlantic vertical motion response and the Hadley cell anomaly shift southward (compared to that in boreal summer) and is mainly centered over the deep tropics south of 10°N (Supplementary Fig. 1), the boreal winter North Atlantic cold SST horseshoe pattern remains similar to that in boreal summer, which locates mainly north of 10°N (Supplementary Fig. 7b). This indicates that the anomalous Hadley cell and associated subsidence is not the cause of the North Atlantic cold SST horseshoe pattern.

The transient evolution of the response in the upper ocean heat budget components over two key regions relevant to the horseshoe structure, i.e., the eastern boundary over the northern (southern) subtropical North Atlantic (see locations in Supplementary Fig. 8a), further supports the importance of oceanic advective processes relative to atmospheric (net downward surface heat flux) processes. Here, annual mean fields are used for the heat budget analyses to avoid any potential seasonal heat storage/accumulation effect. Over both of these two key regions (Supplementary Fig. 8b, c), the response in upper-ocean heat content tendency is mostly negative, indicating cooling of the upper ocean. Over these regions, the total ocean heat transport convergence (OHTC) response is negative and dominated by the contribution from the anomalous horizontal advective OHTC. The positive net downward surface heat flux response (warming) acts as negative feedback (i.e., a damping term) for the upper ocean cooling and gradually counters the OHTC reduction (cooling), so that the averaged response in the upper ocean heat content tendency becomes weaker for the last 40 years (Supplementary Fig. 8b, c). These results support the key role of oceanic advective processes in driving the upper subtropical North Atlantic eastern boundary cooling.

The temporal evolution of the boreal summer cold SAT anomalies along the horseshoe pathway in the water hosing ensemble also exhibits a similar noticeable delay (Fig. 2d), indicating that the cold SAT anomalies along the horseshoe pathway are affected by ocean processes through air–sea heat flux exchange. Since the second decade, the cold extratropical upper ocean temperature anomalies advected by the North Atlantic subtropical gyre along the eastern side of the horseshoe pathway are damped by the positive F_{SFC} anomalies (i.e., reduced air–sea heat fluxes released from the ocean into the atmosphere) there (Fig. 4f–h). The positive F_{SFC} anomalies (Fig. 3b) contribute to the cold SAT anomalies along the eastern side of the horseshoe pathway (Fig. 2b). The advection of the cold extratropical SAT anomalies (induced by ocean processes as discussed earlier) by the eastern branch of the climatological mean boreal summer atmospheric subtropical anticyclone (which coincides with the horseshoe pathway,

Fig. 2b) may also contribute to the propagation of the cold SAT anomalies along the horseshoe pathway and the westward spread of the relatively stronger cold SAT anomalies formed over the eastern side of the horseshoe pathway (Fig. 2b). Meanwhile, the anomalies in the near-surface winds along most parts of the horseshoe pathway are negligible (Fig. 3e), indicating that the WES feedback is not crucial for the equatorward propagation of the cold extratropical signal along the horseshoe pathway.

Over the deep tropical North Atlantic, the relationship between boreal summer F_{SFC} and SST anomalies changes spatially (Supplementary Fig. 7a). Between ~2°N and 6°N, positive F_{SFC} anomalies coincide with relatively weak warm SST anomalies. However, between ~6°N and 10°N, positive F_{SFC} anomalies coincide with cold SST anomalies, which is inconsistent with the spatial pattern expected from the WES feedback (Supplementary Fig. 7a). Further north, between ~11°N and 18°N, regions of relatively weak cold SST anomalies correspond with negative F_{SFC} anomalies, which might suggest a WES feedback signature. However, the decomposition of the anomalous F_{SFC} components (Supplementary Fig. 9) indicates that the negative F_{SFC} anomalies, particularly over the central tropical North Atlantic (magenta box in Supplementary Fig. 9e), is also driven by reduction in the net downward shortwave radiation (Supplementary Fig. 9b, f) linked to the increase in low-level cloud cover (Supplementary Fig. 10c), rather just by the enhanced latent heat flux alone (Supplementary Fig. 9a, f). While this net downward shortwave radiation reduction is partially offset by the enhanced net downward longwave radiation (Supplementary Fig. 9b, d, f), the total net downward radiation reduction still exceeds the magnitude of the enhanced latent heat flux (Supplementary Fig. 9f). The total enhanced turbulent heat flux (latent plus sensible) is comparable to the magnitude of the total net downward radiation reduction (Supplementary Fig. 9f). These findings suggest that cloud radiative feedback also plays a role in the net downward surface heat flux response over the central tropical North Atlantic.

The boreal summer warm SST/SAT anomalies over the tropical South Atlantic and associated equatorward anomalies in the upper tropical North Atlantic western boundary current

In the water hosing ensemble, while cold North Atlantic SST anomalies develop along the horseshoe pathway, warm SST anomalies develop over the tropical South Atlantic (Fig. 3a) during boreal summer. The surface warming response over the tropical South Atlantic is associated with enhanced Atlantic Ocean heat transport convergence (Supplementary Fig. 2), which is balanced by negative F_{SFC} anomalies (i.e., more heat flux is released from the ocean into the atmosphere) over this region (Fig. 3b). The negative F_{SFC} anomalies provide negative feedback (i.e., damping effect) to the warm SST anomalies and induce warm SAT anomalies over the tropical South Atlantic (Fig. 3d).

Over the tropical South Atlantic in boreal summer (i.e., austral winter), the upper ocean is less stratified and there is more background wind-driven turbulent vertical mixing and upwelling in the upper ocean compared to that in boreal winter (i.e., austral summer)²⁹. Hence, in the water hosing ensemble, the warm SST anomalies in the tropical South Atlantic in boreal summer are affected more by the warm thermocline temperature anomalies in the tropical Atlantic (Supplementary Figs. 7a, 11a) through vertical mixing and upwelling, compared to those in boreal winter. In contrast, the warm SST anomalies over the tropical South Atlantic in boreal winter are less affected by the warm thermocline temperature anomalies and are weaker than those in boreal summer (Supplementary Figs. 7b, 11b).

As introduced earlier, the AMOC weakening induces warm thermocline temperature anomalies in the tropical Atlantic through oceanic wave adjustments³⁰. The wave adjustments contribute to the equatorward anomalies in the upper tropical Atlantic western boundary current (Fig. 6a–d). The equatorward anomalies in the upper tropical Atlantic western boundary current (Fig. 7c) is consistent with the reduction in the northward tropical Atlantic Ocean heat transport in the water hosing ensemble (Supplementary Fig. 2). However, the equatorward anomalies in the upper ocean western boundary current around 3°N–10°N are stronger compared to those north of 10°N and south of 3°N (Fig. 7a–c), indicating

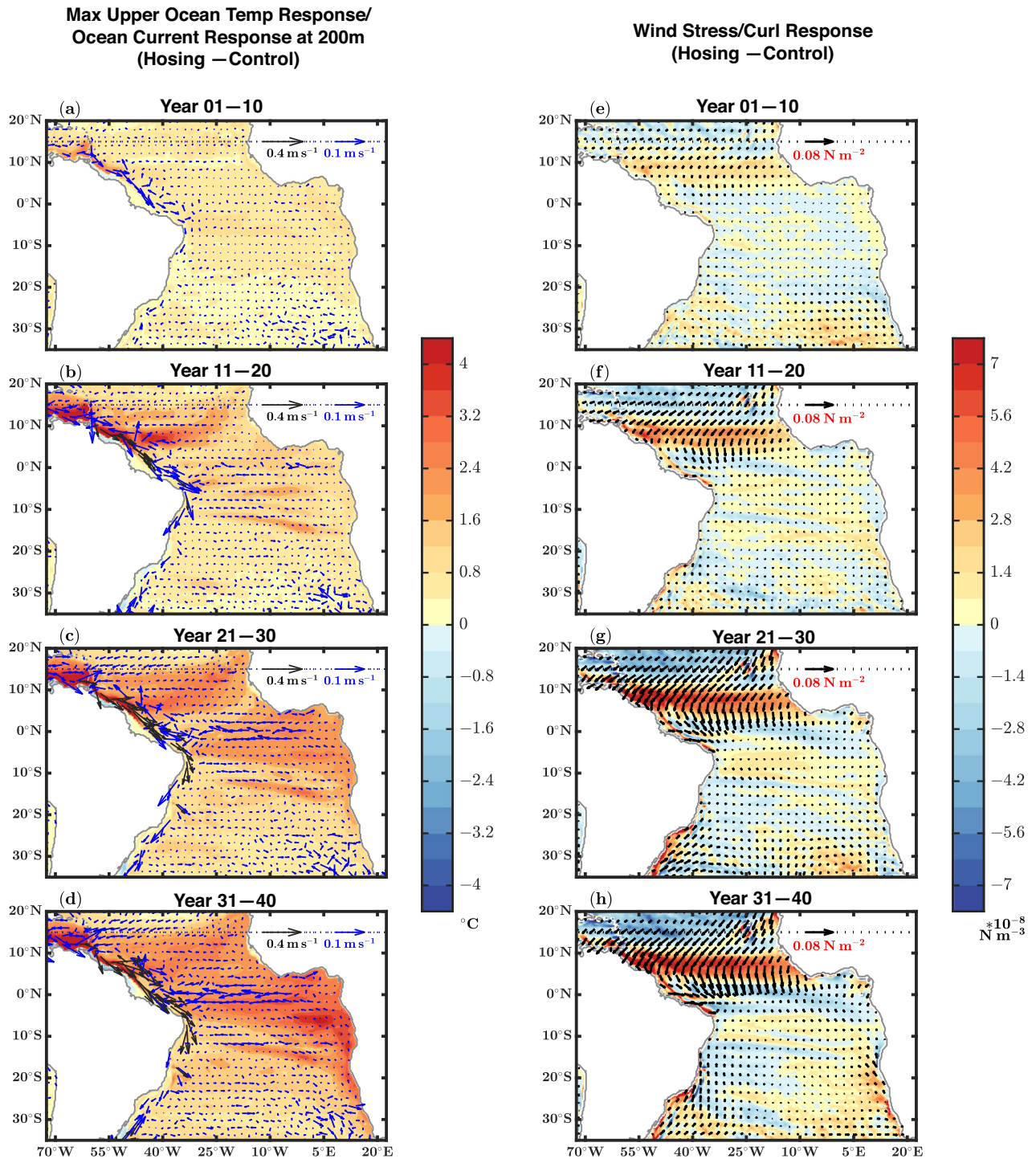


Fig. 6 | Transient boreal summer maximum upper ocean temperature response and transient boreal summer response in ocean current at 200 m and surface wind stress/curl. The response is derived in the same way as in Fig. 4. **a–d** The maximum upper ocean temperature response within the top 500 m (shading)

overlapped with ocean current response at 200 m depth (vector). Vectors greater (less) than 0.1 m s^{-1} in magnitude are shown as black (blue) arrows. **e–h** Surface wind stress curl response (shading) overlapped with surface wind stress response (vector).

that they are not just a direct response to the AMOC weakening. Next, we will show that they are amplified by positive surface wind stress curl anomalies over this region around 3°N – 10°N .

In the water hosing ensemble, when the cold extratropical North Atlantic SST/SAT anomalies propagate equatorward along the horseshoe pathway and the warm SST/SAT anomalies develop over the tropical South Atlantic, there is a pronounced response in trade winds over the tropical Atlantic (Figs. 3a, d, e, 4a–d). Over the tropical North (South) Atlantic, cold

(warm) SST/SAT anomalies are associated with high (low) sea-level pressure (SLP) anomalies (Fig. 3e), creating a strong SLP gradient at the boundary between the dipole SLP anomalies around 10°N , coinciding with the boreal summer climatological convergence zone (Fig. 2b). This SLP gradient intensifies trade winds north of the boundary of the dipole SLP anomalies and weakens trade winds to the south (Fig. 3e). These trade wind anomalies are reflected in surface wind stress anomalies, which produce positive anomalies in surface wind stress curl over the tropical North

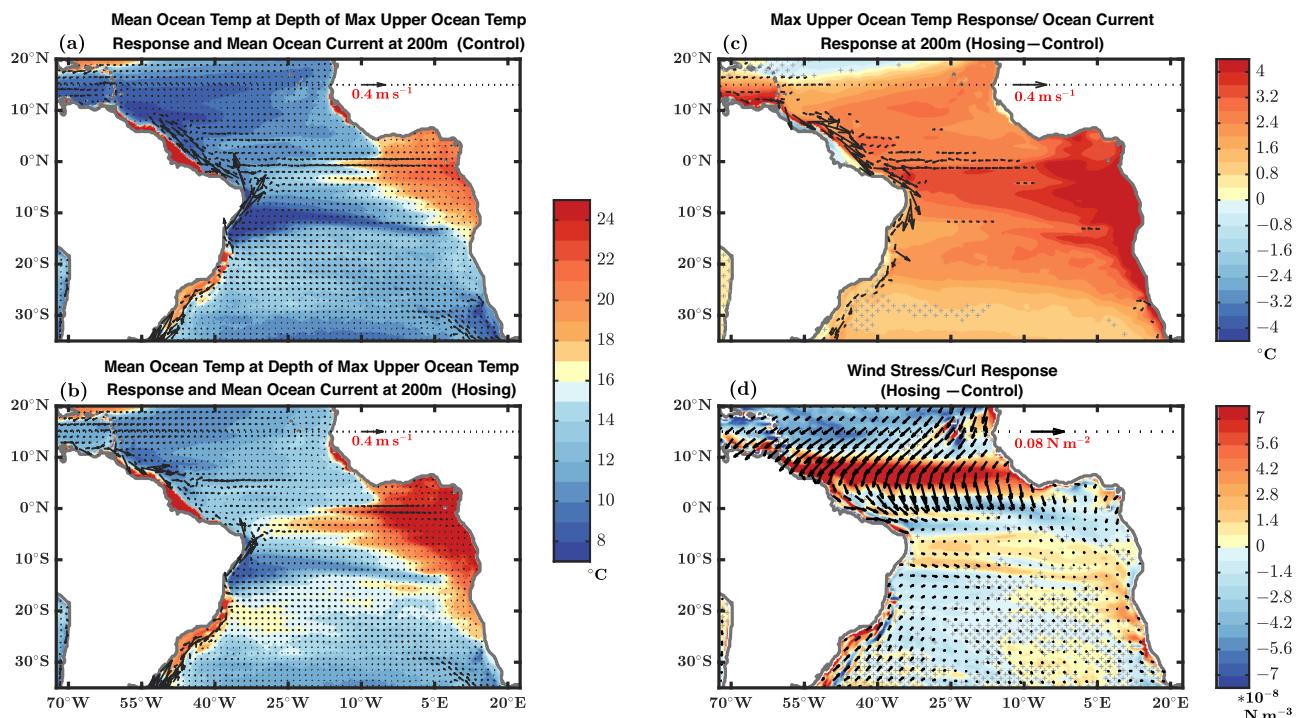


Fig. 7 | Climatological mean upper ocean temperature at the depth of the maximum upper ocean temperature response and climatological mean ocean current at 200 m, along with the long-term mean maximum upper ocean temperature response and the long-term mean response in ocean current at 200 m and surface wind stress/curl, during boreal summer. a, b Climatological mean upper ocean temperature (shading) at the depth of the maximum upper ocean temperature response, overlapped with climatological mean ocean currents at 200 m depth (vector), averaged over the last 40 years of the control and the hosing ensembles,

respectively. **c** Long-term mean maximum upper ocean (top 500 m) temperature response (derived in the same way as in Fig. 6 but averaged over the last 40 years, shading) and ocean current response at 200 m depth (vectors). Vectors less than 3 cm s^{-1} in magnitude are not shown. **d** Long-term mean response in surface wind stress curl (shading) and surface wind stress (vector) averaged over the last 40 years. Stippling (gray color) in (c, d) indicates regions where the variables shown in shading are not significant at the 5% level.

Atlantic around 3°N - 10°N (Fig. 7d). The positive anomalies in surface wind stress curl induce anomalous poleward Sverdrup transport³⁰ in the interior ocean around 3°N - 10°N . For example, the peak Sverdrup transport anomaly integrated from the eastern boundary to the eastern edge of the western boundary ($\sim 42^{\circ}\text{W}$) is $\sim 12 \text{ Sv}$ around 7.5°N . The anomalous poleward Sverdrup transport in the interior ocean has to be balanced by the anomalous equatorward western boundary current, forming an anomalous cyclonic ocean gyre circulation³¹. Hence, the equatorward anomalies in the upper ocean western boundary current around 3°N - 10°N are amplified in addition to those induced directly by the AMOC weakening (Fig. 7c).

In the water hosing ensemble, relatively stronger warm thermocline temperature anomalies first appear near the western boundary between 5°N - 15°N (Fig. 6a, b), where the climatological mean meridional temperature contrast/gradient is relatively strong (Fig. 7a). This response is related to the equatorward advection of the climatological mean warmer thermocline water at the northern side (Fig. 7a) by the anomalous equatorward upper ocean western boundary current around this region (Fig. 6a, b). When the net upper ocean western boundary meridional velocity around 3°N - 10°N becomes equatorward due to both direct AMOC weakening and positive surface wind stress curl anomalies, the relatively stronger warm thermocline temperature anomalies near the western boundary between 5°N - 15°N can be effectively advected equatorward to amplify warm thermocline temperature anomalies in the tropical Atlantic. Hence the strong equatorward anomalies in the upper ocean western boundary current around 3°N - 10°N amplify the warm thermocline temperature anomalies in the tropical Atlantic and associated SST/SAT anomalies over the tropical South Atlantic, which further amplify the positive surface wind stress curl anomalies around 3°N - 10°N , thus provide positive feedback to amplify the equatorward anomalies in the upper ocean western boundary current in this region (Fig. 6). As discussed earlier, the warm SST anomalies over the

tropical South Atlantic are weaker in boreal winter than in boreal summer, thus the positive surface wind stress curl anomalies around 3°N - 10°N and associated equatorward anomalies in the upper ocean western boundary current in this region are also weaker in boreal winter than in boreal summer (Supplementary Figs. 12, 13).

The relationship between the zonally integrated AMOC and NSTC proposed in the previous study²¹ does not explain the amplified equatorward anomalies in the upper ocean western boundary current around 3°N - 10°N and the result that they are stronger in boreal summer than in boreal winter in the water hosing ensemble. In fact, the equatorward subsurface return flow of the zonally integrated NSTC over this region mainly appears in boreal winter rather than in boreal summer in the water hosing ensemble (Supplementary Fig. 11c, d). Here, we identify a novel mechanism to explain the relationship between the AMOC weakening and the amplified equatorward anomalies in the upper tropical North Atlantic western boundary current during boreal summer, through coupled interactions with surface wind stress curl anomalies that amplify the anomalous wind-driven upper ocean western boundary current over the tropical North Atlantic.

As shown in previous studies and discussed earlier, the AMOC weakening induces thermocline deepening along the North Atlantic western boundary through the equatorward propagation of coastal Kelvin waves, which continue eastward along the equator as Kelvin waves and partially propagate westward as Rossby waves in the tropical Atlantic, leading to warm thermocline temperature anomalies over the central and eastern tropical Atlantic^{19,20}. Figure 6a-d shows the transient evolution of the maximum upper ocean temperature response to better illustrate the oceanic wave propagation. The maximum subsurface temperature response appears at different depths around the climatological thermocline at different locations, including the shallower thermocline depth near the eastern equatorial Atlantic, because the wave induced

subsurface temperature response would be strongest around the climatological thermocline depth. The subsurface warming in the tropical South Atlantic already emerges within the first decade (Fig. 6a), consistent with the timescale of the initial wave propagation. As the AMOC continues to weaken over subsequent decades, the warming signal along the western boundary of the tropical North Atlantic (i.e., the source signal) strengthens and is gradually advected equatorward by the anomalous equatorward upper-ocean western boundary current, which then spreads into the eastern and interior tropical Atlantic via wave propagation (Fig. 6b–d). Hence, the maximum temperature response in the tropical South Atlantic gets stronger in subsequent decades as the source signal gets stronger. The spatial pattern of the maximum subsurface warming response (Fig. 6a–d) reveals that the signal propagates to the equator and the eastern boundary along the Kelvin wave pathway and spreads into the interior ocean north and south of the equator by Rossby waves. The transient evolution of temperature anomalies in the eastern South Atlantic along 10°E (Supplementary Fig. 14) indicates that there is a southward propagation of the subsurface warming along the climatological thermocline from the equatorial South Atlantic toward the subtropical South Atlantic, consistent with coastal Kelvin wave propagation. There is stronger subsurface warming along the eastern tropical South Atlantic where the climatological thermocline is shallow and the climatological vertical temperature gradient is strong (Supplementary Fig. 14c, d).

In the quasi-equilibrium state over the last 40 years, the subsurface warming response is spread in the entire tropical South Atlantic, which is much stronger than the magnitude of the corresponding positive SST anomalies over the central and eastern tropical South Atlantic (Figs. 3a, 7c). The basin-averaged temperature response also indicates that between 10°S and 0°S of the tropical South Atlantic, the subsurface temperature anomalies are substantially warmer than the SST anomalies (Supplementary Fig. 11a), consistent with the upwelling of subsurface temperature anomalies to the surface during boreal summer, as elaborated below.

The surface warming response over the tropical South Atlantic is primarily concentrated in the central and eastern basin (Fig. 3a), where there is strong climatological mean wind-driven upwelling in boreal summer. The climatological mean negative surface wind stress curl over the tropical South Atlantic is stronger in boreal summer compared to that in boreal winter, especially over the eastern boundary of the tropical South Atlantic (Supplementary Fig. 15). This corresponds to stronger wind-driven Ekman upwelling over the tropical South Atlantic in boreal summer (compared to that in boreal winter), hence more upwelling of warm subsurface temperature anomalies to the surface in this region. Once the basin-scale central and eastern tropical South Atlantic subsurface warming anomalies are upwelled to the surface, they lead to positive SST and SAT anomalies, which induce the basin-scale negative (low) SLP anomalies over the central and eastern tropical South Atlantic (Fig. 3e). The climatological mean equatorward surface wind stress near the eastern boundary of the tropical South Atlantic is stronger in boreal summer than that in boreal winter (Supplementary Fig. 15), which also leads to stronger westward Ekman transport (to the interior ocean) and thus stronger coastal upwelling near the eastern boundary of the tropical South Atlantic in boreal summer than that in boreal winter. Hence, there is more upwelling of warm subsurface temperature anomalies to the surface along the eastern boundary of the tropical South Atlantic in boreal summer.

Despite the presence of warm subsurface anomalies, the warming SST response over the tropical South Atlantic during boreal winter (i.e., austral summer) is relatively weaker (Supplementary Figs. 7, 11a, b). This seasonal difference aligns with the climatological mean difference in the surface wind stress curl (Supplementary Fig. 15) and associated wind-driven Ekman upwelling and eastern boundary coastal upwelling over the tropical South Atlantic. The weaker and southward shifted boreal winter tropical Atlantic vertical motion response (Supplementary Fig. 1) is related to the weaker warm SST anomalies over the tropical South Atlantic (Supplementary Fig. 7b) during boreal winter, a season with weaker climatological mean wind-driven upwelling.

The transient evolution of the response in the upper ocean heat budget components over the western boundary of the tropical North Atlantic and the eastern boundary of the tropical South Atlantic (see locations in Supplementary Fig. 8a), further supports the importance of oceanic advective processes relative to atmospheric (net downward surface heat flux) processes over these regions. Over the western boundary of the tropical North Atlantic (Supplementary Fig. 8d), the response in the upper ocean heat content tendency is positive (i.e., warming). The total OHTC response is positive and dominated by the contribution from the anomalous horizontal advective OHTC. The net downward surface heat flux response is negative in this region, meaning that the ocean is losing heat to the atmosphere, which acts as a damping term to the warming tendency (Supplementary Fig. 8d). This further supports the key role of oceanic advective processes in driving the upper tropical North Atlantic western boundary warming. Similarly, over the eastern boundary over the tropical South Atlantic (Supplementary Fig. 8e), the response in the upper ocean heat content tendency is positive (i.e., warming), which is forced by the positive total OHTC response dominated by the contribution from the anomalous horizontal advective OHTC. The net downward surface heat flux response is negative in this region and acts as a damping term (i.e., cooling) to the warming tendency (Supplementary Fig. 8e). This again supports the mechanism that the eastern tropical South Atlantic warming is driven by oceanic advective processes.

Mechanisms of the boreal summer Atlantic ITCZ shift

The North Atlantic SST response with a horseshoe pattern and the tropical South Atlantic SST response with an opposite sign in boreal summer are characteristic features of the Atlantic extratropical-tropical teleconnection, leading to the tropical atmospheric response, such as the Atlantic ITCZ shift that we focus on in this subsection.

In the water hosing ensemble, when the cold extratropical North Atlantic SST/SAT anomalies propagate equatorward along the horseshoe pathway and the warm SST/SAT anomalies develop over the tropical South Atlantic (Fig. 4a–d), there is a pronounced response in precipitation over the tropical Atlantic (Fig. 4i–l). The tropical precipitation response represents a southward shift of the Atlantic ITCZ. In the new quasi-equilibrium state, the anomalies in precipitation can be approximated by the anomalies in the column-integrated moisture flux convergence (see “Methods” section), given that the evaporation anomalies (Supplementary Fig. 10a) are much smaller than the precipitation anomalies over the tropical Atlantic where there are strong precipitation anomalies (Fig. 3c). In the water hosing ensemble, the anomalies in the low-level column-integrated moisture flux convergence (from 1000 hPa to 850 hPa, Fig. 3f), which are primarily driven by the contribution from the trade wind anomalies advecting the climatological mean specific humidity (Supplementary Fig. 16), dominate the anomalies in the entire column-integrated moisture flux convergence over the tropical Atlantic (Supplementary Fig. 10b). The contribution from the non-linear term (i.e., the product of change in humidity and change in winds in Eq. 5 in “Methods” section) is negligible. Above the troposphere boundary layer, contributions to the anomalous moisture flux convergence are negligible. Hence, the reduction in precipitation in the northern tropical Atlantic is associated with the anomalous divergence in the low-level column-integrated moisture flux induced by enhanced trade winds, and the increase in precipitation in the southern tropical Atlantic is associated with the anomalous convergence in the low-level column-integrated moisture flux induced by weakened trade winds. The results support a pivotal role of the trade wind response induced by the dipole SST/SAT anomalies over the Atlantic in the southward shift of the Atlantic ITCZ.

Outside the Atlantic, there is also a significant reduction in precipitation over the southern Sahel region, which is again primarily associated with the anomalous divergence in the column-integrated moisture flux (Supplementary Fig. 10b), especially at the low-level (Fig. 3f) that is induced by anomalies in low-level winds (Supplementary Fig. 16a). The trade wind response over the tropical Atlantic reduces the moisture supply to the Sahel

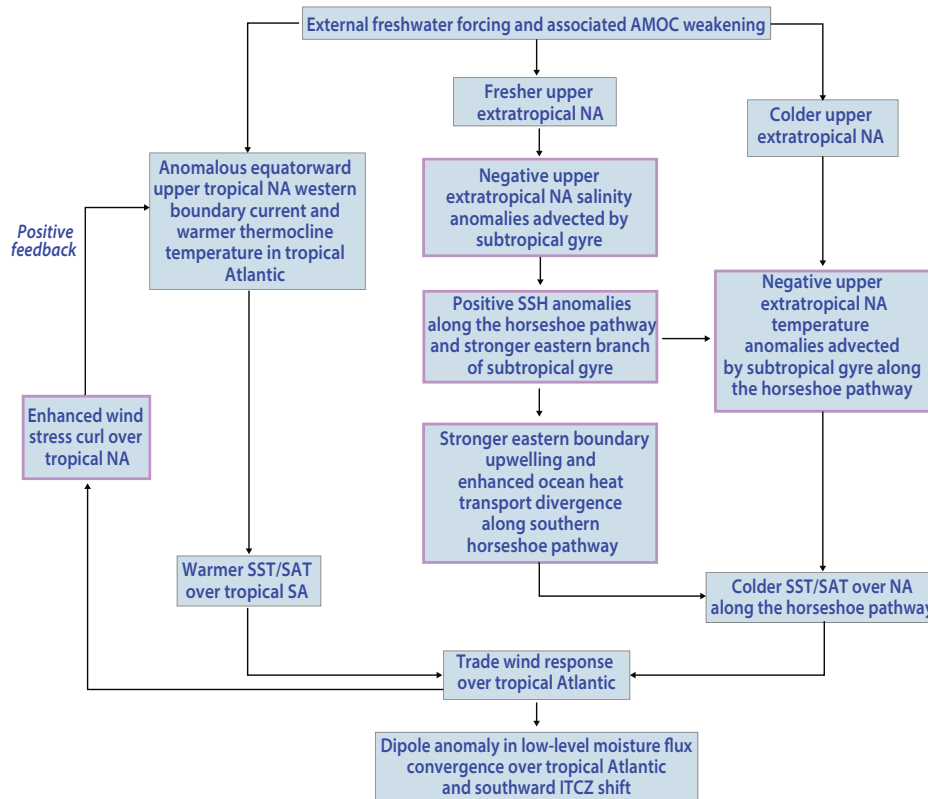


Fig. 8 | Schematic of the Atlantic extratropical-tropical teleconnection during boreal summer in response to external freshwater forcing. The external freshwater forcing leads to the AMOC weakening and reduced northward ocean heat transport into the extratropical North Atlantic (NA), resulting in colder upper extratropical NA ocean temperature. The advection of cold upper extratropical NA temperature anomalies by the subtropical gyre dominates the equatorward propagation of cold upper ocean temperature anomalies along the horseshoe pathway, contributing to cold SST/SAT anomalies along the horseshoe pathway. The external freshwater forcing also leads to pronounced negative upper extratropical NA salinity anomalies, which are advected equatorward by the subtropical gyre and contribute to positive SSH anomalies along the horseshoe pathway. This leads to the strengthening of the eastern branch of the upper subtropical gyre, including the stronger southwestward upper ocean current that induces enhanced eastern boundary upwelling/cooling, and

enhanced ocean heat transport divergence thus amplified cold SST anomalies along the southern horseshoe pathway. The enhanced eastern branch of the upper subtropical gyre also advects the cold extratropical SST anomalies along the horseshoe pathway, in addition to the advection by the mean upper subtropical gyre. The weakened AMOC also leads to anomalous equatorward upper tropical NA western boundary current and warmer thermocline temperature in the tropical Atlantic, contributing to warmer SST/SAT over the tropical South Atlantic (SA). The dipole Atlantic SST/SAT anomalies lead to the trade wind response, which induces pronounced positive surface wind stress curl anomalies over the tropical NA, providing positive feedback to the anomalous equatorward upper tropical NA western boundary current and associated warm SST/SAT anomalies over the tropical SA in the hosing ensemble. The trade wind response drives a southward Atlantic ITCZ shift through the dipole anomaly in the low-level moisture flux convergence over the tropical Atlantic.

region and contributes to reduced evaporation (Supplementary Fig. 10a) and thus enhanced surface warming over the northern Sahel (Fig. 3a, d). The widespread surface cooling response north of Sahel and the surface warming response over the northern Sahel induce the dipole SLP anomalies (i.e., high SLP anomalies to the north and low SLP anomalies to the south) across the northern boundary of the Sahel, which weaken the southwesterly surface winds there (Fig. 3e) and provide positive feedback to reduced evaporation over the northern Sahel. In the water hosing ensemble, there is also an increase (decrease) in the low-level cloud over the North Atlantic (Sahel) due to the surface cooling (warming) response (Supplementary Fig. 10c). The increase (decrease) in the low-level cloud could provide positive feedback to the surface cooling (warming) response by reflecting more (less) shortwave radiation. Therefore, low cloud feedback could amplify the surface temperature response and associated ITCZ shift response as found in the previous study¹⁶.

Discussion

In this study, we conducted an idealized water hosing ensemble using a high-resolution climate model with 0.6 Sv of external freshwater forcing applied over in the southern Nordic Seas to understand the Atlantic extratropical-tropical teleconnection during boreal summer, when the Atlantic ITCZ shift is most pronounced.

The schematic diagram (Fig. 8) summarizes the identified key mechanisms behind the Atlantic extratropical-tropical teleconnection during boreal summer. The external freshwater forcing leads to the AMOC weakening and reduced northward ocean heat transport into the extratropical North Atlantic, resulting in colder SST/reduced surface turbulent heat fluxes, and thus colder SAT over the extratropical North Atlantic. In the water hosing ensemble, the advection of cold upper extratropical North Atlantic temperature anomalies by the North Atlantic subtropical gyre dominates the equatorward propagation of cold upper ocean temperature anomalies along the horseshoe pathway, contributing to cold SST/SAT anomalies along the horseshoe pathway. The external freshwater forcing also leads to pronounced negative upper extratropical North Atlantic salinity anomalies, which are advected equatorward by the North Atlantic subtropical gyre and contribute to positive SSH anomalies along the horseshoe pathway. This leads to the strengthening of the eastern branch of the upper North Atlantic subtropical gyre, including the stronger southwestward upper ocean current that induces enhanced eastern boundary upwelling/cooling, and enhanced ocean heat transport divergence thus amplified cold SST anomalies along the southern horseshoe pathway. The enhanced eastern branch of the upper North Atlantic subtropical gyre also advects the cold extratropical SST anomalies along the horseshoe pathway, in addition to the advection by the mean upper North Atlantic subtropical

gyre. The weakened AMOC also leads to anomalous equatorward upper tropical North Atlantic western boundary current and warmer thermocline temperature in the tropical Atlantic, contributing to warmer SST/SAT over the tropical South Atlantic. The dipole Atlantic SST/SAT anomalies lead to the trade wind response, which enhances surface wind stress curl over the tropical North Atlantic, providing positive feedback to the anomalous equatorward upper tropical North Atlantic western boundary current and associated warm SST/SAT anomalies over the tropical South Atlantic. The trade wind response drives a southward Atlantic ITCZ shift through the dipole anomaly in the low-level moisture flux convergence over the tropical Atlantic.

Contrary to some previous studies using slab ocean models coupled with AGCMs that attribute the equatorward spread of the extratropical North Atlantic surface cooling to positive WES feedback^{17,18}, our results using a fully coupled model reveal no significant wind changes along most parts of the North Atlantic horseshoe pathway (Fig. 3e), suggesting that WES feedback is not the primary mechanism driving the North Atlantic SST/SAT horseshoe pattern during boreal summer. Instead, we find that the advection by the North Atlantic subtropical gyre of the upper extratropical North Atlantic signal is a key mechanism driving the boreal summer North Atlantic SST/SAT horseshoe pattern in the water hosing ensemble. The slab ocean models used in some previous studies cannot represent key oceanic processes, such as the advection of upper-ocean temperature and salinity along the horseshoe pathway, which is crucial for the North Atlantic horseshoe pattern in response to strong external freshwater forcing. Additionally, the surface warming response over the tropical South Atlantic simulated in our full coupled model involves oceanic processes (e.g., western boundary current response and eastern boundary upwelling) that cannot be represented by slab ocean models. Even in a previous study³² using an AGCM coupled to a slab ocean model, turning off the WES feedback had no significant impact on the equatorward propagation of the extratropical response over the North Atlantic sector. In contrast, the most significant differences caused by turning off the WES feedback is over the Pacific, suggesting that other mechanisms may contribute to the equatorward spread of the extratropical signal over the North Atlantic in the AGCM coupled to a slab ocean model³². The equatorward advection of cold extratropical SAT anomalies by the climatological mean anticyclonic surface winds in boreal summer likely also plays a role among other mechanisms.

In the water hosing ensemble, the enhanced low-level clouds also amplify the Atlantic extratropical-tropical teleconnection as found in the previous study¹⁶. The strengthened tropical North Atlantic trade winds may deepen the tropical North Atlantic mixed layer, providing positive feedback to the tropical North Atlantic surface cooling³³ and the Atlantic ITCZ shift³⁴. The energy budget framework, which involves a compensation between anomalous cross-equatorial northward ocean and atmosphere heat transport, has been proposed for the extratropical-tropical teleconnection^{5,14–16}. In the energy budget framework, the reduction of the northward ocean heat transport in the tropics is compensated by the increase in the northward atmosphere heat transport, which is linked to the anomalous Hadley circulation. However, the energy budget framework does not explicitly explain the transient evolution of the anomalous western boundary current that causes the reduction of the northward Atlantic ocean heat transport in the tropics. The zonally integrated energy budget framework also does not explain the transient evolution of the zonally asymmetric North Atlantic SST/SAT horseshoe pattern with stronger cooling along the eastern boundary or the coupled interaction between the anomalous upper ocean western boundary current and the anomalous positive wind stress curl/cyclonic wind-driven ocean gyre circulation over the tropical North Atlantic under external freshwater forcing. Furthermore, the energy budget framework does not explain the transient evolution of the warm SST anomalies in the tropical South Atlantic and associated different seasonal response, which are linked to upwelling of warm subsurface temperature anomalies in the central and eastern boundary over the tropical South Atlantic. Our findings offer a more process-based understanding of the zonally asymmetric

Atlantic extratropical-tropical teleconnection that complements and extends beyond that inferred from the zonally integrated energy budget framework.

The detailed mechanisms and the relative importance of the oceanic vs. atmospheric processes causing the Atlantic extratropical-tropical teleconnection may also depend nonlinearly on the amplitude of the external freshwater forcing. Interestingly, the southward advection of the subpolar SSS anomalies and associated surface cooling/enhanced SSH along the horseshoe pathway/Canary Current have also been found in water hosing experiments under a much weaker freshwater forcing (0.1 Sv) in multiple coupled models³⁵. The positive feedback found in this study may become much weaker under weaker external freshwater forcing, and the potential nonlinear relationship between the response and the external freshwater forcing amplitude deserves more future investigations. Our results advance the understanding of the Atlantic extratropical-tropical teleconnection. The strength of this teleconnection is likely underestimated in many climate models, including the coupled climate model used in this study^{22,23}, which may partially due to mean state biases in the North Atlantic Current pathway and associated underestimation of the AMOC-related surface turbulent heat flux released over the extratropical North Atlantic^{3,24,36}. It may also be partially related to mean state biases in the pathway and strength of the northeastern branch of the North Atlantic subtropical gyre that contribute to the underestimation of the equatorward oceanic advection of the extratropical North Atlantic signal. Additionally, many climate models underestimate eastern boundary upwelling and inadequately represent thermocline over the tropical eastern South Atlantic³⁷, which may result in an underestimation of the AMOC weakening induced surface warming over the tropical South Atlantic. The strength of the simulated Atlantic extratropical-tropical response may vary across climate models and depend on their specific mean-state biases. Addressing these biases in climate models (including the coupled climate model used in this study^{22,23}) in future studies are likely crucial for accurately capturing the strength of the Atlantic extratropical-tropical teleconnection and associated tropical atmospheric response such as the ITCZ shift.

Methods

Coupled climate model and experiments

For this study, we use the Geophysical Fluid Dynamics Laboratory (GFDL) high-resolution coupled climate model version 4 (CM4C192^{22,23}) with significantly revised ocean bathymetry around the Faroe Bank Channel to have a realistic representation of the Iceland-Scotland overflow strength. CM4C192 has a horizontal resolution of $\sim 0.5^\circ$ in the atmosphere component and $\sim 0.25^\circ$ in the ocean component. We use a constant present-day (1990) radiative forcing for the control simulation. The same constant radiative forcing is used for the water hosing experiments as well. We conduct an idealized water hosing ensemble with 0.6 Sv of the anomalous freshwater flux uniformly distributed over the southern Nordic Seas (64°N to 69°N and 45°W to 20°E) for 80 years, similar to the water hosing approach used in a recent study³⁸. To reduce the influence of internal variability, we conduct three ensemble members initialized from different years of the control simulation for the water hosing ensemble. In response to the prescribed freshwater forcing, the maximum AMOC decreases rapidly in the first 40 years of the water hosing ensemble. Thereafter, the rate of the AMOC slowdown stabilizes. To elucidate the response to the prescribed freshwater forcing, we analyze the ensemble mean and compare it to the corresponding 80-year control ensemble (i.e., the ensemble mean of the three 80-year control simulation segments starting from the same initial conditions). Here, the purpose of ensemble mean is to reduce internal variability produced in individual ensemble member and focus on the ensemble mean response to external freshwater forcing. The last 40 years of the ensembles is used to represent the quasi-equilibrium response. The earlier periods (i.e., years 1–10, 11–20, 21–30, and 31–40) are used to examine the evolution of the transient response. We use the two-sided student *t*-test for the statistical significance testing of the ensemble mean difference between the water hosing and the control ensembles (i.e., the

quasi-equilibrium long-term mean response) averaged over the last 40 years.

Moisture budget analysis

The boreal summer moisture budget equation for the long-term mean state is expressed as the following balance between precipitation minus evaporation and the convergence of column-integrated moisture flux³⁹:

$$\bar{P} - \bar{E} = -\frac{1}{g} \nabla \cdot \int_0^{P_s} \bar{q} \bar{\mathbf{v}} dp \approx -\frac{1}{g} \nabla \cdot \int_0^{P_s} \bar{q} \bar{\mathbf{v}} dp \quad (1)$$

where P is precipitation, E is evaporation, q is specific humidity, \mathbf{v} is the horizontal wind, and $\nabla \cdot \int_0^{P_s} q \mathbf{v} dp$ is the divergence of the column-integrated (from the surface to the top of the atmosphere) moisture flux. The overbar denotes the boreal summer season (JJAS) mean (averaged over the last 40 years of the control/water hosing ensemble). The convergence of the column-integrated mean moisture flux in Eq. (1) signifies the net moisture flux entering and leaving the entire atmospheric column. We ignore the eddy terms in (1) as we focus on the boreal summer season.

Defining Δ as the long-term mean difference between the ensemble mean of the water hosing and the control ensembles, we derive the following equation for the long-term mean difference:

$$\Delta \bar{P} - \Delta \bar{E} = -\frac{1}{g} \nabla \cdot \int_0^{P_s} \Delta(\bar{q} \bar{\mathbf{v}}) dp \approx -\frac{1}{g} \nabla \cdot \int_0^{P_s} \Delta(\bar{q} \bar{\mathbf{v}}) dp \quad (2)$$

The right side of Eq. (2) can be further decomposed to identify the contributions of the long-term mean changes in winds, moisture, and both (winds and moisture) to the total long-term mean change in the convergence of column-integrated moisture flux. Thus, Eq. (2) can be rewritten as:

$$\Delta \bar{P} - \Delta \bar{E} \approx -\frac{1}{g} \left[\nabla \cdot \int_0^{P_s} (\bar{q}_{\text{Control}} \Delta \bar{\mathbf{v}} + \bar{\mathbf{v}}_{\text{Control}} \Delta \bar{q} + \Delta \bar{q} \Delta \bar{\mathbf{v}}) dp \right] \quad (3)$$

In the above Eq. (3), the convergence of the vertical integral of $\bar{q}_{\text{Control}} \Delta \bar{\mathbf{v}}$, $\bar{\mathbf{v}}_{\text{Control}} \Delta \bar{q}$, and $\Delta \bar{q} \Delta \bar{\mathbf{v}}$ denotes the contribution to the convergence of the vertical integral of the long-term mean change in the moisture flux due to the long-term mean changes in winds, humidity, and both winds and humidity, respectively.

We divide the atmospheric column between the top of the atmosphere (~0 hPa) and the surface (~1000 hPa) into three layers: upper (0–500 hPa), mid (500–850 hPa), and lower (850–1000 hPa). The moisture budget Eqs. (2) and (3) for the long-term mean change become:

$$\Delta \bar{P} - \Delta \bar{E} \approx -\frac{1}{g} \left[\nabla \cdot \int_{0 \text{ hPa}}^{500 \text{ hPa}} \Delta(\bar{q} \bar{\mathbf{v}}) dp + \nabla \cdot \int_{500 \text{ hPa}}^{850 \text{ hPa}} \Delta(\bar{q} \bar{\mathbf{v}}) dp + \nabla \cdot \int_{850 \text{ hPa}}^{1000 \text{ hPa}} \Delta(\bar{q} \bar{\mathbf{v}}) dp \right] \quad (4)$$

$$\Delta \bar{P} - \Delta \bar{E} \approx -\frac{1}{g} \left[\nabla \cdot \int_{0 \text{ hPa}}^{500 \text{ hPa}} (\bar{q}_{\text{Control}} \Delta \bar{\mathbf{v}} + \bar{\mathbf{v}}_{\text{Control}} \Delta \bar{q} + \Delta \bar{q} \Delta \bar{\mathbf{v}}) dp + \nabla \cdot \int_{500 \text{ hPa}}^{850 \text{ hPa}} (\bar{q}_{\text{Control}} \Delta \bar{\mathbf{v}} + \bar{\mathbf{v}}_{\text{Control}} \Delta \bar{q} + \Delta \bar{q} \Delta \bar{\mathbf{v}}) dp + \nabla \cdot \int_{850 \text{ hPa}}^{1000 \text{ hPa}} (\bar{q}_{\text{Control}} \Delta \bar{\mathbf{v}} + \bar{\mathbf{v}}_{\text{Control}} \Delta \bar{q} + \Delta \bar{q} \Delta \bar{\mathbf{v}}) dp \right] \quad (5)$$

In Eq. (4), the first, second, and third terms inside the brackets correspond to the long-term mean changes in moisture flux divergence at the upper, mid, and lower atmospheric layers, respectively. This equation provides insight into which layer (upper, mid, or lower) dominates the overall long-term mean change in precipitation minus evaporation. Equation (5), an extended form of Eq. (4), breaks down the convergence of the vertical integral of the long-term mean change in the moisture flux between two pressure levels into three components related $\bar{q}_{\text{Control}} \Delta \bar{\mathbf{v}}$, $\bar{\mathbf{v}}_{\text{Control}} \Delta \bar{q}$, and $\Delta \bar{q} \Delta \bar{\mathbf{v}}$. This breakdown helps to identify which component contributes most to the convergence of the vertical integral of the long-term mean change of

moisture flux at each layer (upper, mid, or lower). We utilize Eq. (5) for our analysis.

Data availability

The key model data used in this study is made available publicly on Zenodo⁴⁰.

Code availability

The code of the Geophysical Fluid Dynamics Laboratory (GFDL) coupled climate model version 4 (CM4) is publicly available at <https://zenodo.org/records/3339397>.

Received: 18 March 2025; Accepted: 1 October 2025;

Published online: 17 November 2025

References

1. Broecker, W. S., Peteet, D. M. & Rind, D. Does the ocean–atmosphere system have more than one stable mode of operation? *Nature* **315**, 21–26 (1985).
2. Rahmstorf, S. Ocean circulation and climate during the past 120,000 years. *Nature* **419**, 207–214 (2002).
3. Zhang, R. et al. A review of the role of the Atlantic meridional overturning circulation in Atlantic multidecadal variability and associated climate impacts. *Rev. Geophys.* **57**, 316–375 (2019).
4. Vellinga, M. & Wood, R. A. Global climatic impacts of a collapse of the Atlantic thermohaline circulation. *Clim. Chang.* **54**, 251–267 (2002).
5. Zhang, R. & Delworth, T. L. Simulated tropical response to a substantial weakening of the Atlantic thermohaline circulation. *J. Clim.* **18**, 1853–1860 (2005).
6. Orihuela-Pinto, B., England, M. H. & Taschetto, A. S. Interbasin and interhemispheric impacts of a collapsed Atlantic overturning circulation. *Nat. Clim. Chang.* **12**, 558–565 (2022).
7. Enfield, D. B., Mestas-Nuñez, A. M. & Trimble, P. J. The Atlantic multidecadal oscillation and its relation to rainfall and river flows in the Continental US. *Geophys. Res. Lett.* **28**, 2077–2080 (2001).
8. Zhang, R. & Delworth, T. L. Impact of Atlantic multidecadal oscillations on India/Sahel rainfall and Atlantic hurricanes. *Geophys. Res. Lett.* **33**, L17712 (2006).
9. Mohino, E., Janicot, S. & Bader, J. Sahel rainfall and decadal to multi-decadal sea surface temperature variability. *Clim. Dyn.* **37**, 419–440 (2011).
10. Dunstone, N. J., Smith, D. M. & Eade, R. Multi-year predictability of the tropical Atlantic atmosphere driven by the high latitude North Atlantic Ocean. *Geophys. Res. Lett.* **38**, L14701 (2011).
11. Ruiz-Barradas, A., Nigam, S. & Kavvada, A. The Atlantic Multidecadal Oscillation in twentieth century climate simulations: uneven progress from CMIP3 to CMIP5. *Clim. Dyn.* **41**, 3301–3315 (2013).
12. Yuan, T. L. et al. Positive low cloud and dust feedbacks amplify tropical North Atlantic Multidecadal Oscillation. *Geophys. Res. Lett.* **43**, 1349–1356 (2016).
13. Kim, W. M., Yeager, S., Chang, P. & Danabasoglu, G. Low-frequency North Atlantic climate variability in the Community Earth System Model large ensemble. *J. Clim.* **31**, 787–813 (2018).
14. Broccoli, A. J., Dahl, K. A. & Stouffer, R. J. Response of the ITCZ to Northern Hemisphere cooling. *Geophys. Res. Lett.* **33**, L01702 (2006).
15. Kang, S. M., Held, I. M., Frierson, D. M. & Zhao, M. The response of the ITCZ to extratropical thermal forcing: Idealized slab-ocean experiments with a GCM. *J. Clim.* **21**, 3521–3532 (2008).
16. Zhang, R., Kang, S. M. & Held, I. M. Sensitivity of climate change induced by the weakening of the Atlantic meridional overturning circulation to cloud feedback. *J. Clim.* **23**, 378–389 (2010).
17. Chiang, J. C. H. & Bitz, C. M. Influence of high latitude ice cover on the marine Intertropical Convergence Zone. *Clim. Dyn.* **25**, 477–496 (2005).

18. Smirnov, D. & Vimont, D. J. Extratropical forcing of tropical Atlantic variability during boreal summer and fall. *J. Clim.* **25**, 2056–2076 (2011).
19. Kawase, M. Establishment of deep ocean circulation driven by deep-water production. *J. Phys. Oceanogr.* **17**, 2297–2317 (1987).
20. Zhang, R. Anticorrelated multidecadal variations between surface and subsurface tropical North Atlantic. *Geophys. Res. Lett.* **34**, L12713 (2007).
21. Chang, P. et al. Oceanic link between abrupt changes in the North Atlantic Ocean and the African monsoon. *Nat. Geosci.* **1**, 444–448 (2008).
22. Held, I. M. et al. Structure and performance of GFDL's CM4.0 climate model. *J. Adv. Model. Earth Syst.* **11**, 3691–3727 (2019).
23. Zhao, M. Simulations of atmospheric rivers, their variability, and response to global warming using GFDL's new high-resolution general circulation model. *J. Clim.* **33**, 10287–10303 (2020).
24. Zhang, R. et al. Sensitivity of the North Atlantic Ocean circulation to an abrupt change in the Nordic Sea overflow in a high resolution global coupled climate model. *J. Geophys. Res.* **116**, C12024 (2011).
25. Yeager, S., Karspeck, A., Danabasoglu, G., Tribbia, J. & Teng, H. A decadal prediction case study: late twentieth-century North Atlantic Ocean heat content. *J. Clim.* **25**, 5173–5189 (2012).
26. Robson, J. I., Sutton, R. T. & Smith, D. M. Initialized decadal predictions of the rapid warming of the North Atlantic Ocean in the mid 1990s. *Geophys. Res. Lett.* **39**, L19713 (2012).
27. Msadek, R. et al. Predicting a decadal shift in North Atlantic climate variability using the GFDL forecast system. *J. Clim.* **27**, 6472–6496 (2014).
28. Kim, W. M., Yeager, S. & Danabasoglu, G. Atlantic multidecadal variability and associated climate impacts initiated by ocean thermohaline dynamics. *J. Clim.* **33**, 1317–1334 (2020).
29. Scannell, H. A. & McPhaden, M. J. Seasonal mixed layer temperature balance in the southeastern tropical Atlantic. *J. Geophys. Res. Oceans* **123**, 5557–5570 (2018).
30. Sverdrup, H. U. Wind-driven currents in a baroclinic ocean; with application to the equatorial currents of the eastern Pacific. *Proc. Natl. Acad. Sci. USA* **33**, 318–326 (1947).
31. Stommel, H. The westward intensification of wind-driven ocean currents. *Trans. Am. Geophys. Union* **29**, 202–206 (1948).
32. Mahajan, S., Saravanan, R. & Chang, P. The role of the wind–evaporation–sea surface temperature (WES) feedback as a thermodynamic pathway for the equatorward propagation of high-latitude sea ice–induced cold anomalies. *J. Clim.* **24**, 1350–1361 (2011).
33. Senapati, B., O'Reilly, C. H. & Robson, J. Pivotal role of mixed-layer depth in tropical Atlantic multidecadal variability. *Geophys. Res. Lett.* **51**, e2024GL110057 (2024).
34. Kataoka, T., Suzuki, T. & Tabebe, H. Rainfall–mixed layer–SST feedback contributing to Atlantic Meridional Mode Development. *J. Clim.* **36**, 899–915 (2023).
35. Swingedouw, D. et al. Decadal fingerprints of fresh water discharge around Greenland in a multi-model ensemble. *Clim. Dyn.* **41**, 695–720 (2013).
36. Joshi, R. & Zhang, R. Impacts of the North Atlantic biases on the upper troposphere/lower stratosphere over the extratropical North Pacific. *npj Clim. Atmos. Sci.* **6**, 151 (2023).
37. Farneti, R., Stiz, A. & Ssebandeke, J. B. Improvements and persistent biases in the southeast tropical Atlantic in CMIP models. *npj Clim. Atmos. Sci.* **5**, 42 (2022).
38. Wei, X. & Zhang, R. Weakening of the AMOC and strengthening of Labrador Sea deep convection in response to external freshwater forcing. *Nat. Commun.* **15**, 10357 (2024).
39. Trenberth, K. E. & Guillemot, C. J. Evaluation of the global atmospheric moisture budget as seen from analyses. *J. Clim.* **8**, 2255–2280 (1995).
40. Joshi, R., & Zhang, R. Supporting Data for On the Atlantic extratropical-tropical teleconnection in response to external freshwater forcing [Data Set]. Zenodo, <https://doi.org/10.5281/zenodo.17243725> (2025).

Acknowledgements

Leo Donner, Ming Zhao, David Paynter and Xiaosong Yang are acknowledged for their helpful comments and suggestions on this work. We thank Catherine Raphael for illustration support. R. J. is supported by Princeton University Graduate School and CIMES Task II funds for graduate research under award NA18OAR4320123 from the National Oceanic and Atmospheric Administration, U.S. Department of Commerce. R. Z. is supported by GFDL base funding. We acknowledge the GFDL resources made available for this research.

Author contributions

R.Z. and R.J. conceived the study and designed the main approaches. R.Z. conducted the numerical experiments. R.J. conducted the analysis of the control and the water hosing ensembles. The authors discussed the results/interpretations and wrote the paper together.

Competing interests

The authors declare no competing interests.

Additional information

Supplementary information The online version contains supplementary material available at <https://doi.org/10.1038/s41612-025-01253-z>.

Correspondence and requests for materials should be addressed to Rajat Joshi or Rong Zhang.

Reprints and permissions information is available at <http://www.nature.com/reprints>

Publisher's note Springer Nature remains neutral with regard to jurisdictional claims in published maps and institutional affiliations.

Open Access This article is licensed under a Creative Commons Attribution 4.0 International License, which permits use, sharing, adaptation, distribution and reproduction in any medium or format, as long as you give appropriate credit to the original author(s) and the source, provide a link to the Creative Commons licence, and indicate if changes were made. The images or other third party material in this article are included in the article's Creative Commons licence, unless indicated otherwise in a credit line to the material. If material is not included in the article's Creative Commons licence and your intended use is not permitted by statutory regulation or exceeds the permitted use, you will need to obtain permission directly from the copyright holder. To view a copy of this licence, visit <http://creativecommons.org/licenses/by/4.0/>.

© The Author(s) 2025